

The classical and quantum dynamics of molecular spins on graphene

Christian Cervetti,^{1} Angelo Rettori² Maria Gloria Pini,³ Andrea Cornia,⁴ Ana Repollés,⁵ Fernando Luis,⁵ Martin Dressel,¹ Stephan Rauschenbach,⁶ Klaus Kern,^{6,7} Marko Burghard⁶ & Lapo Bogani^{1,8*}*

¹ 1. Physikalisches Institut, Universität Stuttgart, Pfaffenwaldring 57, D-70550 Stuttgart (Germany).

² Dipartimento di Fisica, Università di Firenze, Via G. Sansone 1, I-50019 Sesto Fiorentino (Italy).

³ Istituto dei Sistemi Complessi, CNR, Unità di Firenze, Via Madonna del Piano 10, I-50019 Sesto Fiorentino (Italy).

⁴ Dipartimento di Scienze Chimiche e Geologiche, Università di Modena e Reggio Emilia, INSTM RU, Via G. Campi 183, I-41125 Modena (Italy).

⁵ Instituto de Ciencia de Materiales de Aragón, CSIC-Universidad de Zaragoza, C/ Pedro Cerbuna 12, E-50009 Zaragoza (Spain).

⁶ Max-Planck-Institut für Festkörperforschung, Heisenbergstrasse 1, D-70569 Stuttgart (Germany).

⁷ Institut de Physique de la Matière Condensée, Ecole Polytechnique Fédérale de Lausanne (EPFL), CH-1015 Lausanne (Switzerland).

⁸ Department of Materials, University of Oxford, 16 Parks Road, OX1 3PH, Oxford (United Kingdom). e-mail: lapo.bogani@materials.ox.ac.uk

Keywords: graphene, spin dynamics, nanomaterials, quantum tunneling, molecular magnetism.

Controlling the dynamics of spins on surfaces is pivotal to the design of spintronic¹ and quantum computing² devices. Several proposed strategies involve the interaction of spins with graphene³, which would enable surface-state spintronics^{4,5}, coherent spin coupling⁶ and electrical spin manipulation^{5,7-12}. Here we unravel the classical and quantum dynamics of spins on graphene, using molecular magnets¹³. While the static magnetic properties of the molecules remain unaltered, the quantum spin dynamics and associated selection rules are profoundly modulated. The contributions stemming from the coupling of the spin to graphene phonons, other spins, and Dirac fermions are quantified, and reproduced in a newly-developed theoretical framework. Coupling to electrons introduces a dominant quantum-relaxation channel that, by driving the spins over Villain's threshold, gives rise to fully-delocalised, resonant spin tunneling. Our findings provide fundamental insight into the interaction between spins and graphene, and establish the experimental and theoretical basis for the electrical manipulation of spins in graphene nanodevices.

Carbon-based spintronics offers a mean to electrically manipulate localized spins in close proximity of a carbon nanotube¹⁴⁻¹⁶ or graphene sheet^{3,5,7-12}. This task requires understanding and tuning of the interaction

between the components, in order to improve the spin performance, e.g. by minimizing quantum-decoherence¹⁷, and to enable spin manipulation, e.g. by controlling either the magnetic anisotropy¹⁸ or the electronic coupling¹⁹. However, there is currently little understanding of how the spin states in such devices are affected by the environment. Here, we exploit the exceptionally-clean magnetic features of single-molecule-magnets (SMMs)¹³ to explore how spins interact with graphene substrates.

The graphene-SMM hybrids are obtained by non-covalent grafting of the SMM $[\text{Fe}_4(\text{L})_2(\text{dpm})_6]$, (Hdpm=dipivaloylmethane and $\text{H}_3\text{L}=2\text{-(hydroxymethyl)-2-}\{[(4\text{-(pyren-1-yl)-butoxy)methyl}\}\text{propane-1,3-diol}$, Fig.1a)²⁰ via solution-based assembly onto exfoliated graphene sheets. The two pyrene groups serve as anchors²⁰ to the graphene sheet. Functionalization of both solid-supported and bulk dispersions of graphene layers (Methods) allows determining the aggregation behaviour of the molecules on graphene and performing magnetization measurements on statistically-relevant samples.

Atomic force microscopy (AFM) confirms successful decoration of graphene by $[\text{Fe}_4(\text{L})_2(\text{dpm})_6]$ (Fig.1b). Similar coverage was observed for single-, double- or multi-layer graphene. Sufficiently low concentrations of $[\text{Fe}_4(\text{L})_2(\text{dpm})_6]$ ($C < 10^{-6}$ M) ensure graphene decoration by individual molecules without appreciable aggregation, while a full layer is formed for $C > 10^{-5}$ M (SI). Multiple techniques show that the deposited SMMs are structurally and electronically intact. In particular, the height distribution in AFM images is peaked at 1.8 ± 0.3 nm (Fig.1c), in close agreement with the size of individual $[\text{Fe}_4(\text{L})_2(\text{dpm})_6]$ molecules.²⁰ In addition, Raman spectra (Fig.1d) exhibit only a small up-shift of the G-band by ~ 4 cm^{-1} with respect to bare graphene, indicating very slight p-type doping.²¹ This conclusion is also supported by the small positive shift of the charge-neutrality-point observed in the resistance vs. gate voltage curves (Fig.s1e,f), indicating a charge-transfer of only $0.08 e^-$ per SMM. Furthermore, X-ray photoelectron spectra display the same characteristic peak positions of thin films of $[\text{Fe}_4(\text{L})_2(\text{dpm})_6]$ (SI) and mass spectra evidence clear fingerprints of intact $[\text{Fe}_4(\text{L})_2(\text{dpm})_6]$ at 1919, 1763 and 1736 amu (Fig.1g).

The static magnetic properties of the hybrids are indistinguishable from those of crystalline $[\text{Fe}_4(\text{L})_2(\text{dpm})_6]$ (Fig.2). The temperature (T) dependence of the $\chi_m T$ curve (where χ_m is the static molar magnetic susceptibility, obtained from the ratio between magnetization M and the applied magnetic field H) displays the same minimum at 100 K and a maximum around 6 K (Fig.2a, SI). The M vs H curves also match, within experimental error. The characteristic $\chi_m T$ curve can be fitted by considering the Landé factor $g=2.00 \pm 0.05$ and two intramolecular exchange interactions between nearest-neighbour and next-nearest-neighbour Fe(III) ions ($J_{\text{NN}}=-14.85 \pm 0.05$ and $J_{\text{NNN}}=-0.09 \pm 0.05$ cm^{-1} , respectively), in excellent agreement with previous investigations, leading to a total molecular spin ground state $S=5$.

The low-temperature magnetic properties of SMMs are dominated by the presence of a large magnetic anisotropy¹², which lifts the degeneracy of the $S=5$ multiplet and creates an energy barrier ΔE

separating the $|m_s\rangle$ sublevels (Fig.3a). Two spin-relaxation mechanisms are thus possible: a classical overbarrier process, where multiple phonon absorptions allow overcoming ΔE , and a quantum tunneling (QT) mechanism, which is active between degenerate levels at opposite sides of the barrier and can be suppressed by lifting the degeneracy of the $|m_s\rangle$ levels with H . Thus, by applying H , one can separately examine the effect of graphene on both mechanisms.

The magnetization dynamics is probed by measuring the real (χ') and imaginary (χ'') response to a small magnetic field oscillating at frequency ω . In a static field $H=1$ kOe (Fig.3b), when thermally-activated processes are dominant, isolated molecules on graphene show a faster magnetization dynamics than the crystalline $[\text{Fe}_4(\text{L})_2(\text{dpm})_6]$, for which Arrhenius analysis yields a barrier $\Delta E=9.7\pm 0.7$ cm $^{-1}$. In $H=0$ (Fig.3c), all $|m_s\rangle$ and $|-m_s\rangle$ sublevels fall back into resonance and QT is activated, magnifying enormously the differences between the hybrids and crystals. The T -dependence of the spin relaxation time, τ , (Fig.4a) shows that the thermally-activated region persists down to 800 mK for crystalline $[\text{Fe}_4(\text{L})_2(\text{dpm})_6]$, below which temperature QT sets in. This contrasts strikingly with the spin relaxation in the hybrids, where the behaviour is fully dominated by QT, and the QT-rate is about one million times higher (10^5 instead of 10^{-1} Hz).

To explain these observations we subdivide the spin anisotropy into different contributions, with each term having the symmetry of a corresponding tesseral harmonic. This approach produces an intuitive but rigorous picture of the spin behaviour via the Hamiltonian:

$$H = \mu_B g \mu H + \sum_{j=0}^{22} B_j^j \hat{O}_j^j \quad (1)$$

where the first term describes the Zeeman interaction and the second accounts for the magnetic anisotropy via the \hat{O}_i^j spin operators that correspond to the different harmonics, each weighted by a coefficient B_i^j . These operators, called Stevens operator-equivalents,^{12,22} contain the j^{th} power of the spin ladder operators, \hat{S}_+ and \hat{S}_- , and the $(i-j)^{\text{th}}$ power of \hat{S}_z (see SI for explicit expressions and a pictorial representation of the associated harmonics). With equation 1 we can intuitively describe the effect of any external electric field (e.g. the electron density of an underlying substrate) by introducing in the sum a term of corresponding symmetry^{12,22} and discarding all terms not belonging to the point group of the spin environment. Stevens operator-equivalents have an intuitive effect on both classical and quantum relaxation channels: \hat{O}_i^j terms with $j=0$ contain powers of only \hat{S}_z , and contribute to ΔE but do not mix the $|m_s\rangle$ eigenstates; terms with $j\neq 0$, on the contrary, mix states differing in m_s by a multiple of j , opening

the QT relaxation channel. We can now apply this analysis to the case of $[\text{Fe}_4(\text{L})_2(\text{dpm})_6]$.

For crystalline $[\text{Fe}_4(\text{L})_2(\text{dpm})_6]$, $\mathbf{H} = B_2^0 \hat{O}_2^0 + B_2^2 \hat{O}_2^2 + B_4^0 \hat{O}_4^0 + B_4^3 \hat{O}_4^3 + \mu_B S g H$, so that $\Delta E \cong 3 |B_2^0| S_z^2$. Spectroscopic and magnetic investigations yield $B_2^0 = -0.136 \pm 0.003 \text{ cm}^{-1}$, $B_2^2 = 8.1 \pm 0.7 \cdot 10^{-3} \text{ cm}^{-1}$, $B_4^0 = 2.4 \pm 0.5 \cdot 10^{-5} \text{ cm}^{-1}$, and $g = 2.000 \pm 0.005$. From multiple spectroscopic and magnetic investigations on related systems B_4^3 is determined to be $< 5 \pm 1 \cdot 10^{-4} \text{ cm}^{-1}$. By using $g = 2.004 \pm 0.003$ and $B_2^0 = -0.12 \pm 0.02 \text{ cm}^{-1}$, we can perfectly reproduce the magnetization curves of both hybrids and crystals (Fig.2b), and the barrier values extracted from the dynamics provide $B_2^0 = -0.13 \pm 0.01 \text{ cm}^{-1}$, again leading to an excellent overall agreement for the leading axial anisotropy term. Axial distortion of the SMMs on graphene must thus be excluded.

We now show how the graphene environment alters the spin relaxation (Fig.4b), by extending available theoretical treatments.^{23,24} Dipolar and hyperfine interactions introduce a local dynamic magnetic field distribution that alters the QT rate by broadening the QT resonances^{12,25} (Fig.3a). These distributions have been determined, in crystals, from dilution and nuclear resonance experiments²⁷ and are ~ 200 and 1 Oe wide, respectively. Intermolecular dipolar interactions are strongly reduced in the hybrids, because of the sizeable molecular separation and magnetic shielding by graphene, which is predicted to be extremely efficient²⁶. On the contrary, hyperfine interactions arise from the nuclei inside the molecules themselves, and are unaffected by the deposition. This imposes an intrinsic limit of $\sim 10 \text{ Hz}$ to the QT-rate of isolated $[\text{Fe}_4(\text{L})_2(\text{dpm})_6]$ (Fig.4a),^{12,25} and all additional accelerations of the QT must arise from interaction with the graphene layer.

To evaluate the effect of graphene vibrations, we need to extend the existing theoretical background to two-dimensional phonon baths (see SI7). **In principle, the effect of phonons on each molecular group is to induce a time-dependent modification (or "modulation") of any term of the magnetic energy. However, it can be shown¹³ that, at low temperatures, the modulation of the isotropic exchange does not induce transitions between the $|m_s\rangle$ sublevels of the lowest exchange multiplet. Therefore, as in our experiments we are interested in temperatures much lower than the Debye temperature, the only significant contribution will arise from the modulation of the anisotropy energy induced by long-wavelength acoustic phonons.** The transition probabilities can be obtained by^{23,24} adding

to equation 1 the spin-phonon perturbation term $\mathbf{H}_{SP} = i \sum_{q,\lambda} \sqrt{\frac{\hbar}{2m_c \omega_{q,\lambda}}} V_{q,\lambda}(\mathbf{S})(C_{q,\lambda} - C_{q,\lambda}^\dagger)$, where ω , q and λ are the phonon frequency, wavevector and polarization, \hbar Planck constant, m_c the unit cell mass, $V_{q,\lambda}$ the spin-phonon interaction potential, $C_{q,\lambda}$ the phonon creation operator and the sum runs over the Brillouin zone. The relevant phonon bath of the hybrids can then be described with the long-wavelength spectrum of the

acoustic branches of graphene, which has an analytical expression²¹. Phonons produce time-dependent structural transformations of the molecules, introducing local strain and rotation that are transmitted to the spin via spin-orbit coupling. For intact molecules, similar local distortions are expected in both crystals and hybrids and, provided that B_2^0 is essentially unaltered, as in the present case, $V_{q,\lambda}$ will also be similar in both materials. On the contrary, the different phonon densities of three- and two-dimensional baths will strongly alter the relaxation dynamics. Under these assumptions we obtain (see SI) the following relation:

$$\frac{R_c}{R_h} = \frac{2}{3} \frac{\rho_h k_B}{\rho_c \pi} \frac{C_h^4}{C_c^5} \quad (3)$$

where c and h subscripts indicate crystals and hybrids, R a parameter proportional to the experimentally-observable phonon-induced relaxation rate, ρ the mass density, C the sound velocity and k_B is Boltzmann constant. This treatment provides excellent agreement with the data in $H \neq 0$, where the relaxation is expected to be dominated by phonon interactions (Fig.3b), simultaneously accounting for the behaviour of both crystals and hybrids. Remarkably, no fitting parameter is necessary, and full, quantitative agreement is obtained by using the aforementioned B_i^j coefficients and introducing the known speed of sound of graphene²¹, $C_h = 2 \cdot 10^4$ m/s, for the hybrids. It is also noteworthy that the behaviour of crystalline $[\text{Fe}_4(\text{L})_2(\text{dpm})_6]$ is largely restored in samples with large SMM aggregates, where the vibrational bath more closely resembles that of crystals (SI). These observations underscore the relevance of graphene vibrational modes for classical spin relaxation.

By contrast, the different phonon bath cannot explain the striking enhancement of QT at $H=0$ (Fig.4a), which requires introducing the coupling to graphene electrons. The latter is expressed, in Stevens' formalism^{12,22}, by including the perturbation integral $\langle m_s(\psi_M) | V_I | \psi_G \rangle$, where molecular and

graphene electronic states (ψ_M and ψ_G , respectively) interact via the potential V_I , altering the $\left| m_s \right\rangle$ spin state. The wavefunction ψ_G has threefold symmetry, and the corresponding point-group rules²² permit non-vanishing integral terms only for B_i^j coefficients with j a multiple of 3, independently of the form of V_I . In the perturbation treatment of the spin-graphene interaction, all such terms have an identical effect on the level mixing and the QT rate of the lowest $\left| m_s \right\rangle$ levels, differing only in the perturbation order. For QT purposes, we merge all terms into an effective overall graphene effect represented by $B_4^3 \hat{O}_4^3 = B_4^3 \left[\hat{S}_z (\hat{S}_+^3 + \hat{S}_-^3) + (\hat{S}_+^3 + \hat{S}_-^3) \hat{S}_z \right] / 4$, which directly admixes the $m_s = \pm 3$ states, with lower levels

requiring lower symmetry terms, such as $B_2^2 \hat{O}_2^2$. By introducing a $B_4^3 > 2 \cdot 10^{-3} \text{ cm}^{-1}$ term into the simulations, while keeping all other parameters as in the $H \neq 0$ case, both the ac susceptibility peak (Fig.3c) and the T -dependence of τ (Fig.4a) are indeed excellently reproduced. A pictorial representation of the spin anisotropy in the crystals and hybrids (Fig.4c) shows the significant weight of the additional \hat{O}_4^3 term and highlights the signature of the threefold rotational symmetry of graphene on the spin anisotropy. The correct operator form of the microscopic interaction potential for V_I is debated, with several proposals considering scattering processes, described by the operator $\hat{\Xi} = (\hat{S}_+ \hat{\sigma}_- + \hat{S}_- \hat{\sigma}_+ + 2\hat{S}_z \hat{\sigma}_z) / 2$. For $[\text{Fe}_4(\text{L})_2(\text{dpm})_6]$ a direct quantitative comparison among the different proposals is intricate, because of the cumbersome *ab initio* evaluation of the amplitude cross-sections. Anyway, spin-flip processes as efficient as those observed are only predicted when scattering due to the presence of two K points is included in the theory^{27,28}, and the values here obtained can be used to validate the theoretical models proposed for spin-Dirac fermion interactions^{29,30}.

Strongly-perturbative QT of spins, predicted by Villain decades ago¹³, strictly requires pronounced electronic perturbations combined with minimal dipolar interactions. These conditions are hard to fulfil in crystals, and the quantum spin dynamics of Villain's regime has so far eluded observation; graphene hybrids offer ideal conditions by simultaneously suppressing dipolar interactions and enhancing the transverse terms electronically. With suppressed dipolar fields, weak perturbations (as in crystals) lead to a non-monotonic behaviour in the τ vs T plot, where standard tunnelling is followed by a slow descent into Villain's QT regime (SI). In comparison, the B_4^3 perturbation term introduced by graphene is large enough to directly drive the spins into Villain's regime (Fig.4d). The associated threshold yields a lower bound of 0.3 μeV for the interaction between SMM spins and the Dirac electrons, lower than the estimated spin-orbit coupling in graphene.

To conclude, our observations set the theoretical and experimental background for the exploration of the magnetic effects introduced by localized spins in graphene. The clear roles of the vibrational and electronic interactions, here unravelled, can now be exploited in the design of spin-nanomechanical and nanospintronic devices. The presence of strong graphene-induced terms allows envisaging coherent electric spin manipulation (e.g. via electrically-tuned spin mixing), allowing molecular spin control in ways now reserved to other qubits,^{23,27,28} with an observed interaction already introducing a spin-level mixing comparable to those used for qubit manipulations.^{27,28} The use of molecular magnets with even higher spin-orbit coupling (e.g. rare-earths) could enhance such effects even further and similar effects, with the same symmetry, can also be envisaged for other systems, e.g. SMMs on reconstructed Au surfaces.¹⁹ Villain's tunneling regime, being by definition coherent, opens also novel perspectives for quantum operations. Eventually, the observation of substrate effects on the quantum dynamics constitutes

an important methodological tool, which can be applied to study other spin-substrate interactions, providing unique details on symmetry-breaking quantum effects.

Methods Summary

[Fe₄(L)₂(dpm)₆] was synthesized as previously reported²⁴. Graphene was mechanically exfoliated from highly-oriented pyrolytic graphite onto Si/SiO₂ substrates. Surface hybrids were obtained by immersion in a solution of [Fe₄(L)₂(dpm)₆] in 1,2-dichloroethane:dichloromethane (9/1, v/v) at room temperature, followed by washing with isopropanol. Bulk samples of the hybrids were prepared by first sonicating 8.4 mg of graphite powder in 20 ml of the solvent mixture for 48 hrs, followed by adding 11.5 mg of [Fe₄(L)₂(dpm)₆] in 20 ml of the same mixture, followed by stirring for 45 min and final filtering through PTFE membranes (0.2 μm pore size). Magnetic measurements were corrected for the diamagnetism of the sample and sample holder, as independently determined. A home-built micro-SQUID susceptometer inside a dilution refrigerator was used for zero-field measurements, with extremely small ac field amplitudes (50 mOe) and the data corrected by the bare graphene signal. AFM images were acquired with a Bruker ICon system in tapping mode, using silicon cantilevers. MALDI-TOF spectra were recorded using a laser pulsed at ~4 Hz and XPS spectra were obtained on single flakes with a monochromatized Al-Kα source (1486.6 eV), see SI for details. Electronic devices were fabricated using a PMMA resist, e-beam lithography and thermally evaporated Au.

Acknowledgments

We thank J. Wrachtrup and E. Rastelli for discussions, M. Konuma, U. Stützel, J. Sesé, A. L. Barra, D. Drung, Th. Schurig and L. Sebeke for assistance with the measurements and financial support from Italian MIUR, Spanish MINECO (MAT2012-38318-C03-01), BW-Stiftung (Kompetenznetz Funktionelle Nanostrukturen), ERC-StG-338258 "OptoQMol", [the Royal Society \(URF fellowship and grant\)](#) and the AvH Stiftung (Sofja Kovalevskaja award).

Author contributions

C.C. performed the functionalization and most measurements. A.C. produced the molecules. C.C. and S.R. acquired the MALDI-TOF spectra. A.R. and F.L. performed the very-low-temperature magnetic measurements. A.R., M.G.P. and L.B. performed the theoretical analysis. L.B. and M.B. conceived the experiments. L.B. wrote the draft and all authors contributed to discussions and the final manuscript.

Additional information

The authors declare no competing financial interests. Supplementary information (SI) accompanies this paper at www.nature.com.

References

1. Sanvito, S. Organic spintronics: Filtering spins with molecules. *Nature Mater.* **10**, 484–485 (2011).
2. DiVincenzo, D. P. Quantum computation. *Science* **270**, 255-261 (1995).
3. Pesin, D. & MacDonald, A. H. Spintronics and pseudospintronics in graphene and topological insulators. *Nature Mater.* **11**, 409–416 (2012).
4. Han, W., Kawakami, R. K., Gmitra, M., Fabian, M., Graphene spintronics. *Nature Nano.* **9**, 794–807 (2014).
5. Tuan, D. Van, Ortmann, F., Soriano, D., Valenzuela, S. O. & Roche, S. Pseudospin-driven spin relaxation mechanism in graphene. *Nat. Phys.* **10**, 857–863 (2014).
6. Garnica, M., *et al.* Long-range magnetic order in a purely organic 2D layer adsorbed on epitaxial graphene. *Nature Phys.* **9**, 368-374 (2013).
7. Nair, R.R., *et al.* Dual origin of defect magnetism in graphene and its reversible switching by molecular doping. *Nature Comm.* **4**, 2010 (2013).
8. Chen, J. J.-H., Li, L., Cullen, W. G. W., Williams, E. D. E. & Fuhrer, M. S. Tunable Kondo effect in graphene with defects. *Nature Phys.* **7**, 535–538 (2011).
9. Nair, R. R. *et al.* Spin-half paramagnetism in graphene induced by point defects. *Nature Phys.* **8**, 199–202 (2012).
10. Tombros, N. Jozsa, C. Popinciuc, M. Jonkman, H. T. & van Wees, B. J. Electronic spin transport and spin precession in single graphene layers at room temperature. *Nature* **448**, 571–574 (2007).
11. McCreary, K.M., Swartz, A.G., Han, W., Fabian, J. & Kawakami, R. J., Magnetic Moment Formation in Graphene Detected by Scattering of Pure Spin Currents. *Phys. Rev. Lett.* **109**, 186604 (2012).
12. Dlubak, B. *et al.*, A. Highly efficient spin transport in epitaxial graphene on SiC. *Nature Phys.* **8**, 557 (2012).
13. Gatteschi, D., Sessoli, R. & Villain, J. *Molecular Nanomagnets* (Oxford University Press, Oxford, 2006)
14. Hueso, L. E., *et al.* Transformation of spin information into large electrical signals using carbon nanotubes. *Nature* **445**, 410-413 (2007).
15. Laird, E.A., Pei, F. & Kouwenhoven, L.P. A valley-spin qubit in a carbon nanotube. *Nature Nano.* **8**, 565-568 (2013).
16. Kuemmeth, F., Ilani, S., Ralph, D. C. & McEuen, P. L. Coupling of Spin and Orbital Motion of Electrons in Carbon Nanotubes. *Nature* **452** 448-452 (2008).
17. Warner, M. *et al.* Potential for spin-based information processing in a thin-film molecular semiconductor. *Nature* **503**, 504-508 (2013).

18. Oberg, J. C., Calvo, M. R., Delgado, F., Moro-Lagare, M., Serrante, D., Jacob, D., Fernández-Rossier, J., Hirjibeddin, C. F. Control of single-spin magnetic anisotropy by exchange coupling. *Nature Nano.* **9**, 64-68 (2014).
19. Mannini, M., *et al.* Quantum tunneling of the magnetization in a monolayer of oriented single-molecule magnets. *Nature* **468**, 417-421 (2010).
20. Bogani, L., Danieli, C., Biavardi, E., Bendiab, N., Barra, A. L., Dalcanale, E., Wernsdorfer, W. & Cornia, A. Single-molecule-magnets carbon-nanotube hybrids. *Angew. Chem. Int. Ed.* **121**, 760-764 (2009).
21. Ferrari, A. C. & Basko, D. M. Raman spectroscopy as a versatile tool for studying the properties of graphene. *Nature Nano.* **8**, 235–246 (2013).
22. Misra, S. K., Poole, C. P & Farach, H. A. A review of spin Hamiltonian forms for various point-group site symmetries. *Appl. Magn. Reson.* **11**, 29-46 (1996).
23. Fort, A., Rettori, A., Villain, J., Gatteschi, D. & Sessoli, R. Mixed Quantum-Thermal Relaxation in Mn₁₂ Acetate Molecules. *Phys. Rev. Lett.* **80**, 612-615 (1998).
24. Leuenberger, M. N. & Loss, D. Spin tunneling and phonon-assisted relaxation in Mn₁₂-acetate. *Phys. Rev. B* **61**, 1286-1302 (2000).
25. A. Repollés, A. Cornia, F. Luis Spin-lattice relaxation via quantum tunneling in diluted crystals of Fe₄ single-molecule magnets. *Phys. Rev. B* **89**, 054429 (2014).
26. Koshino, M., Arimura, Y. & Ando, T. Magnetic field screening and mirroring in graphene. *Phys. Rev. Lett.* **102**, 177203 (2009).
27. Devoret, M. H. & Schoelkopf, R. J. Superconducting Circuits for Quantum Information: An Outlook. *Science* **339**, 1169-1174 (2013).
28. Yamamoto, M., Takada, S., Bäuerle, C., Watanabe, K., Wieck, A. D. & Tarucha, S. Electrical control of a solid-state flying qubit. *Nature Nano.* **7**, 247 (2012).
29. Trauzettel, B., Bulaev, D. V., Loss, D. & Burkard, G. Spin qubits in graphene quantum dots. *Nat. Phys.* **3**, 192-196 (2007).
30. Lundberg, M. B. Yang, R. Renard, J. & Folk, J. A. Defect-mediated spin relaxation and dephasing in graphene. *Phys. Rev. Lett.* **110**, 156601 (2013).

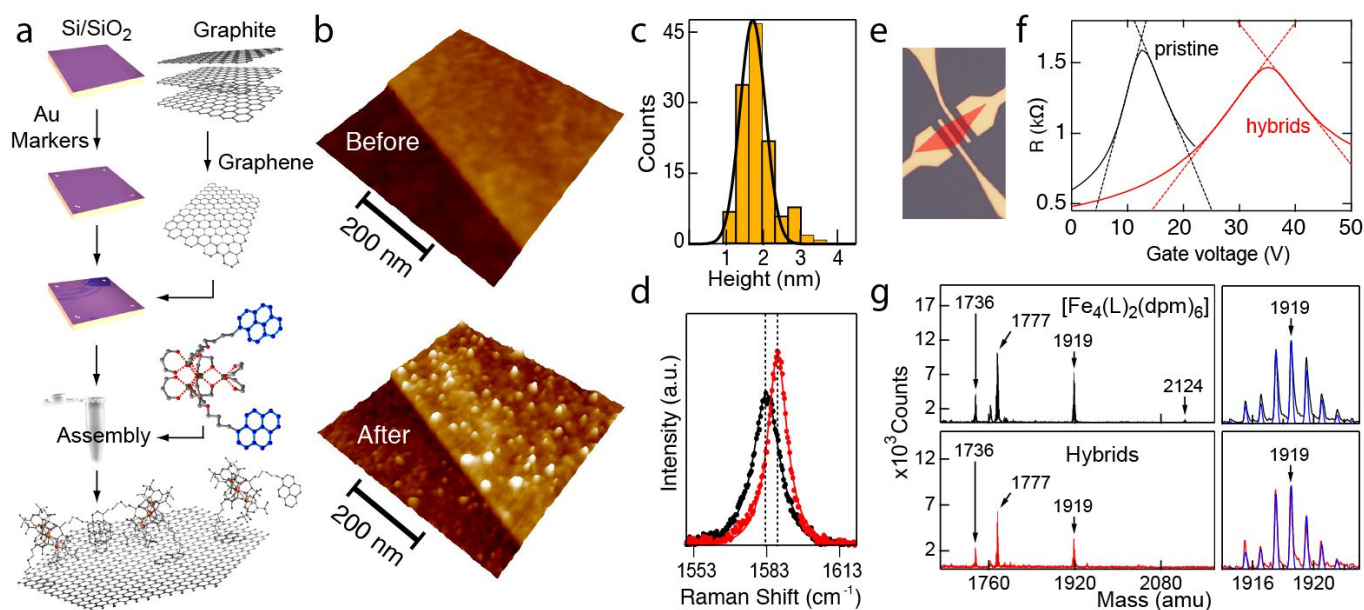


Figure 1. The graphene-spin hybrids. a) Grafting of the molecular magnets on graphene and crystal structure of $[\text{Fe}_4(\text{L})_2(\text{dpm})_6]$ (pyrene groups highlighted in blue, hydrogens and t-butyl groups omitted). b) AFM images of graphene flakes before and after grafting, at $C=2.5 \cdot 10^{-8}$ M. c) AFM height distribution for sub-monolayer coverage and Gaussian fitting, indicating a mean value of 1.85 nm. d) Raman G band, acquired with a 632.8 nm laser at the centre of an exfoliated graphene flake, before (black) and after (red) functionalization at $C=10^{-4}$ M. Lines are fits to the data with Lorentzian curves. e) Optical image of a typical device, with the graphene flake outlined in red. f) Gate dependence of the four-terminal resistance for a single-flake graphene field-effect transistor, for pristine graphene (black) and after grafting (red), at $C=10^{-4}$ M. g) MALDI-TOF spectra of crystalline $[\text{Fe}_4(\text{L})_2(\text{dpm})_6]$ (top) and of the hybrids (bottom), and zoom-in on one isotropic pattern. Blue lines are simulations for intact cluster cores.

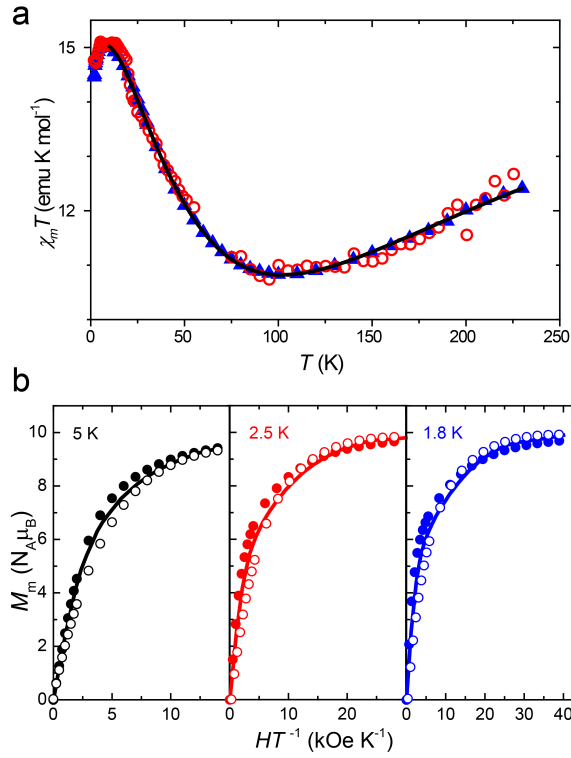


Figure 2. Static magnetic properties of the hybrids a) Temperature dependence of the $\chi_m T$ product of for $[\text{Fe}_4(\text{L})_2(\text{dpm})_6]^{20}$ (triangles) and the hybrids (circles) (measured in $H=1$ kOe for the hybrids and $H=1$ kOe below 30 K and in 10 kOe above for the crystals). The black line represents fitting by considering the intact $[\text{Fe}_4(\text{L})_2(\text{dpm})_6]$ core (see text and Ref. 20). b) Comparison of the low-temperature magnetization curves of crystalline $[\text{Fe}_4(\text{L})_2(\text{dpm})_6]$ (solid points) and the graphene hybrids (open dots), showing the M_m vs H/T curves acquired at 5 K (left), 2.5 K (middle) and 1.8 K (right) after subtracting the graphene matrix contribution and rescaling by the number of $[\text{Fe}_4(\text{L})_2(\text{dpm})_6]$ molecules. Solid lines are fits to the data (see text and Ref. 20).

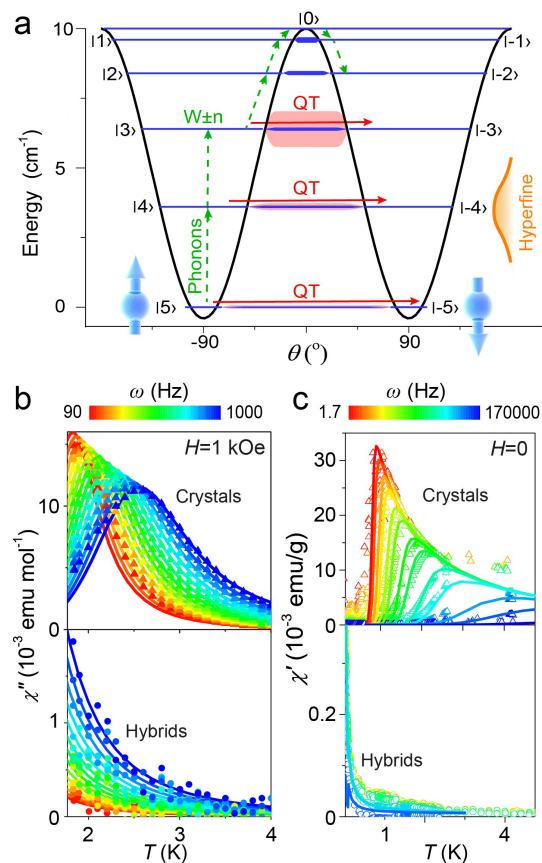


Figure 3. Classical and quantum magnetization dynamics. a) $|m_s\rangle$ sublevels of the ground state of the single-molecule-magnet $[\text{Fe}_4(\text{L})_2(\text{dpm})_6]$, as obtained from equation 1. Phonons determine transition probabilities (green arrows) to thermally overcome the barrier. Quantum tunneling happens between admixed levels (red arrows), while hyperfine and dipolar interactions create energy distributions (orange). Interaction with Dirac electrons increases the tunnel splittings below $|3\rangle$ and $|-3\rangle$ (red areas, exaggerated for clarity). b) Temperature and frequency dependence of the imaginary component of the dynamic susceptibility (χ'') in a magnetic field $H=1$ kOe for $[\text{Fe}_4(\text{L})_2(\text{dpm})_6]$ (top) and hybrids with isolated molecules (bottom). Lines are simulations (see text for the theory). c) Temperature and frequency dependence of the real component of the dynamic susceptibility (χ') in $H=0$ for $[\text{Fe}_4(\text{L})_2(\text{dpm})_6]$ (top) and hybrids with isolated molecules (bottom). Lines are simulations (see text for the theory).

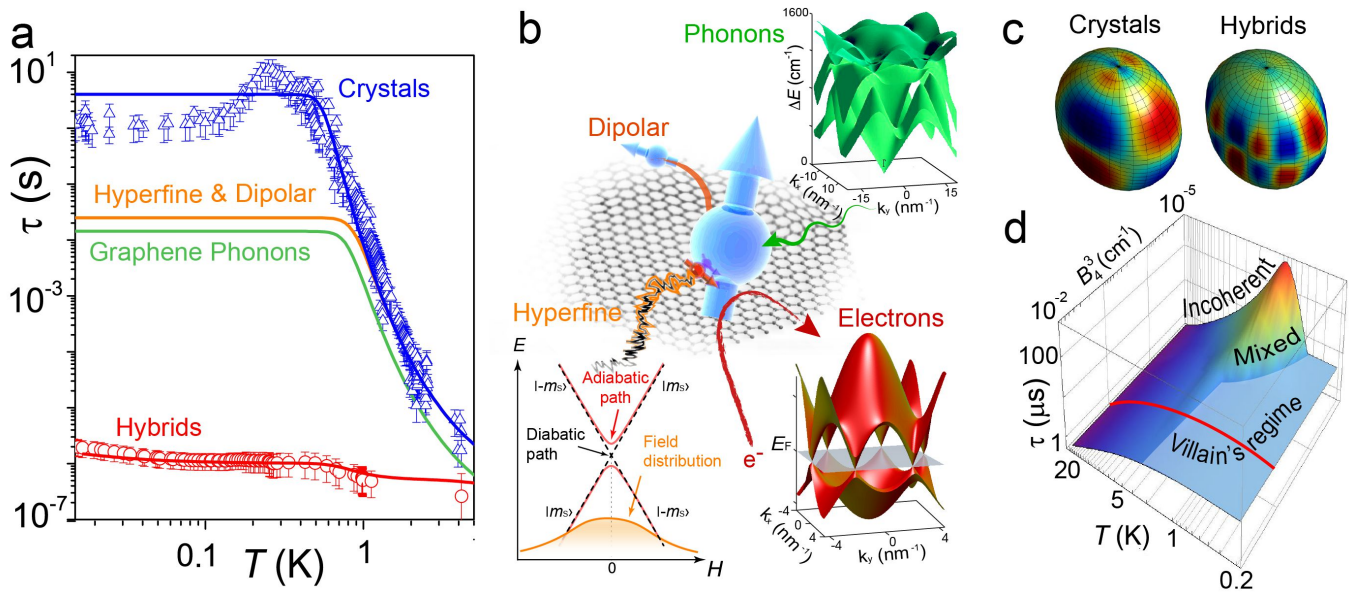


Figure 4. Contributions to the zero-field spin dynamics. a) Temperature dependence of the spin relaxation time in $H=0$, for: $[\text{Fe}_4(\text{L})_2(\text{dpm})_6]$ (blue) and the hybrids (red). Lines show the curves for **0.3 Hz** tunneling **frequency**, and **estimations** of suppressed dipolar interactions (orange), graphene phonons (green) and Dirac electrons-spin interactions (red). b) Different contributions to relaxation lifetime of spins on graphene: The dipolar and hyperfine interactions produce dynamic field distributions around all avoided level crossings (orange); transition probabilities are determined by the graphene phonon dispersion (green surface); Dirac electrons (red surface) introduce quantum mixing terms with fingerprint symmetry. c) Representation of the resulting magnetic anisotropy for $[\text{Fe}_4(\text{L})_2(\text{dpm})_6]$ and the hybrids, visualizing the $B_4^3 \hat{O}_4^3$ term arising from interactions with Dirac electrons. B_2^0 is decreased tenfold for clarity. d) Different tunneling regimes, as a function of temperature and of the strength of the perturbative driving term B_4^3 . The **regime of the hybrids** is highlighted in red.